JOURNAL OF APPLIED CRYSTALLOGRAPHY
ISSN 1600-5767

Effects of polyvinylpyrrolidone on the crystallization of amorphous griseofulvin: fracture and molecular mobility

Yanan Wang,[a,b] Chai-Yee Chin,[b] Naveen Kumar Hawala Shivashekaregowda[b,c]* and Qin Shi[a]*

[a]School of Pharmacy, Jiangsu Vocational College of Medicine, Yancheng 224005, People's Republic of China, [b]School of Pharmacy, Faculty of Health and Medical Science, Taylor's University, Subang Jaya 47500, Malaysia, and [c]Digital Health and Medical Advancement Impact Laboratory, Taylor's University, Subang Jaya 47500, Malaysia. *Correspondence e-mail: navigcp@gmail.com, sqzyf1314@163.com

Received 27 February 2024
Accepted 26 April 2024

Edited by F. Meilleur, Oak Ridge National Laboratory, USA, and North Carolina State University, USA

Keywords: fracture; crystallization; molecular mobility; surfaces; griseofulvin; polyvinylpyrrolidone; crystal growth.

This study aims to investigate the fracture, molecular mobility and crystallization behaviors of amorphous griseofulvin (GSF) in the presence of polyvinylpyrrolidone (PVP). In the presence of 10%(*w*/*w*) PVP K90, the fracture resistance of griseofulvin was greatly improved. Compared with the pure GSF system, the average fracture temperature of the griseofulvin–PVP K90 system was decreased to approximately −6.1°C. More importantly, a statistical study revealed that the direct connection between fracture and nucleation of griseofulvin was weakened in the presence of PVP K90. This study also explored the effects of PVP K90 on the molecular dynamics and crystallization behaviors of amorphous GSF. In the presence of PVP K90, the crystal growth kinetics and molecular dynamics were both slowed down. Interestingly, needle-like crystal growth was observed, exhibiting approximately the same rates as the bubble-induced process. These findings are important for understanding the complex mechanisms of physical stability of polymer-based amorphous solid dispersions.

1. Introduction

As drug discovery becomes more successful, an increasing number of drug candidates and new chemical entities have been found to suffer the problem of poor water solubility (Kalepu & Nekkanti, 2015). One of the most promising approaches for enhancing the solubility of poorly water-soluble drugs is to use their amorphous form (Taylor & Zhang, 2016; Yu, 2001; Shi, Li *et al.*, 2020; Shi, Wang, Moinuddin *et al.*, 2022). However, amorphous solids tend to crystallize because of their higher energy, thus losing the advantages in solubility and dissolution (Zhang, Guo *et al.*, 2023). More importantly, recent studies revealed that crystallization can be much faster at a free surface or interface in comparison with the rates in the interior of amorphous pharmaceutical solids (Shi, Tao *et al.*, 2020; Yu, 2016; Zhang, Xu *et al.*, 2023).

One of the widely used formulation strategies for maintaining the physical stability of amorphous drugs is to disperse them into a polymer matrix (Zhang, Guo *et al.*, 2023; Shi, Chen *et al.*, 2022; Newman & Zografi, 2021). Polymers have been widely reported to affect the nucleation, crystal growth and phase separation of amorphous drugs (Zhang, Guo *et al.*, 2023; Shi, Chen *et al.*, 2022; Sun *et al.*, 2012). The physical stability of polymer-based amorphous pharmaceutical solids can be determined by the physical and chemical properties of the polymer. Ongoing investigations have proposed various mechanisms by which polymers affect the crystallization of amorphous drugs (Cai *et al.*, 2011; Powell *et al.*, 2013; Kestur &

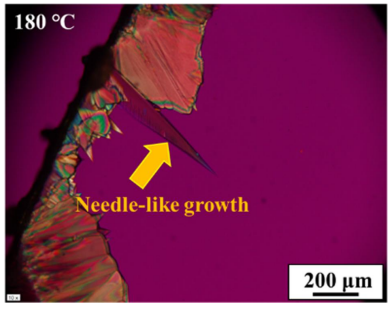

Taylor, 2013; Mistry & Suryanarayanan, 2016). Molecular interactions between drug and polymer are also found to be an important factor for maintaining the physical stability of amorphous solids (Kestur & Taylor, 2010; Trasi & Taylor, 2012*a*). For instance, Taylor and co-workers reported that a decrease in the crystal growth rates of amorphous drugs correlated well with the strength/extent of drug–polymer hydrogen-bonding interactions (Kestur & Taylor, 2010; Trasi & Taylor, 2012*a*). They concluded that polymers with strong hydrogen-bonding acceptors appeared to be more effective inhibitors than those with strong donor groups, even though the model drugs had both hydrogen-bonding donors and acceptors (Trasi & Taylor, 2012*b*). Another mechanism proposed by Yu *et al.* concerned the segmental mobility of polymers in affecting the crystallization of amorphous solids (Powell *et al.*, 2013; Huang, Powell *et al.*, 2017). Huang, Powell *et al.* (2017) reported that the polymer effects on the crystal growth rate of nifedipine and *o*-terphenyl followed one master curve as a function of $(T_{g,polymer} - T_{g,host})/T_{cryst}$, where T_{cryst} represents the temperature for crystal growth and $T_{g,polymer}$ and $T_{g,host}$ represent the glass transition temperatures of the polymer and host molecules, respectively. They proposed that a local polymer-rich region can be created in the process of crystal growth. Prior to participating in the crystalline phase, host molecules must traverse these polymer-rich regions at rates that are determined by the segmental mobility of the polymer (Huang, Powell *et al.*, 2017).

It is well accepted that drug molecules at a free surface or interface exhibit different degrees of freedom in comparison with those in the interior of amorphous pharmaceutical solids (Shi, Tao *et al.*, 2020; Yu, 2016; Shi, Moinuddin *et al.*, 2022). As a result, crystal growth and nucleation at the free surface and interface can be much faster compared with those in the interior (Shi, Tao *et al.*, 2020; Zhang, Xu *et al.*, 2023; Shi *et al.*, 2021; Shi & Cai, 2016; Shi, Wang, Xu *et al.*, 2022) For instance Zhang, Xu *et al.* (2023) investigated the effects of proximity to the surface on the nucleation of clotrimazole polymorphs by using a two-stage method. Compared with bulk nucleation, nucleation rates at the surface of clotrimazole polymorphs were vastly accelerated by 5–6.5 orders of magnitude (Zhang, Xu *et al.*, 2023). Cracks and bubbles in the interior of amorphous solids have also been demonstrated to accelerate crystal growth in the interior of amorphous solids (Shi, Wang, Xu *et al.*, 2022; Powell *et al.*, 2015). More importantly, formation of air–liquid or air–solid interfaces in the interior can favor heterogeneous nucleation, thus resulting in a ripple effect on crystallization.

Griseofulvin (GSF), a classic antifungal drug, is one of the model systems that have been used for exploring the physical stability and dissolution behaviors of amorphous pharmaceutical solids (Shi & Cai, 2016). An extensive statistical study revealed a direct connection between crystal nucleation of griseofulvin and fractures created by cooling (Su *et al.*, 2019). Polyvinylpyrrolidone (PVP) is a polymer showing different molecular weights ranging from 2500 to 3 000 000 Da, which is commonly used as a polymeric carrier for the preparation of amorphous solid dispersions (ASDs) (Zhang, Guo *et al.*, 2023). The *K* value of PVP, representing the average degree of polymerization, ranges from 12 to 120. It is widely reported that ASDs prepared with PVP generally exhibit higher solubility and dissolution for poorly water-soluble drugs (Konno *et al.*, 2008; Pui *et al.*, 2018). In a very recent study, the polymer topology of PVP was demonstrated as the key factor for affecting drug–polymer interactions. Compared with the star-shaped form, linear PVP exhibited more substantial impacts on inhibiting drug crystallization (Orszulak *et al.*, 2024). One goal of the present work was to explore the effects of 10%(*w*/*w*) PVP K90 on the fracture resistance of amorphous griseofulvin and the connections between fracture and crystal nucleation by a statistical study. In addition, the effects of 10%(*w*/*w*) PVP K90 on the crystal growth behavior, kinetics, and liquid dynamics of amorphous GSF were systematically investigated.

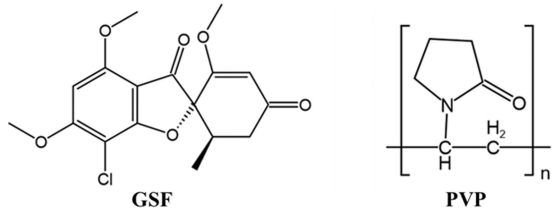

2. Experimental

2.1. Materials

GSF was purchased from J&K Scientific Co. Ltd. PVP K90 (1000–2000 kg mol^{-1}) was obtained from BASF. The drug and polymer were used as received.

2.2. Preparation of PVP K90-doped GSF binary systems

PVP K90-doped GSF systems were prepared by cryogenic milling (JXFSTPRP-MiniCL cryo-miller, Shanghai Jingxin Industrial Development Co. Ltd), an effective approach for obtaining uniform drug–polymer mixtures. GSF systems containing 10%(*w*/*w*) PVP K90 were prepared by mechanically blending 0.1 g of PVP K90 and 0.9 g of pure crystalline GSF at 10 Hz for five cycles. Prior to the milling process, the samples were pre-cooled for 20 min. The time of the milling and cool-down process was 2 min.

2.3. Thermal analysis

Differential scanning calorimetry (DSC) measurements were conducted in a sealed aluminium pan by using a DSC 250 unit (TA Instruments, New Castle, DE, USA) under a 50 ml min^{-1} N_2 purge. This instrument was calibrated for temperature and enthalpy using indium. For the thermal analysis, a total of 6–7 mg of pure GSF powder or PVP K90-doped GSF powder was loaded in the aluminium pan. For the investigation of the probability of fracture and crystallization at different cooling temperatures (T_c), pure griseofulvin and PVP K90-doped griseofulvin powders were first heated to 230°C and isothermally held for 10 min in Run 1 (Fig. 1). For Run 2, these melt samples were cooled at a cooling rate of

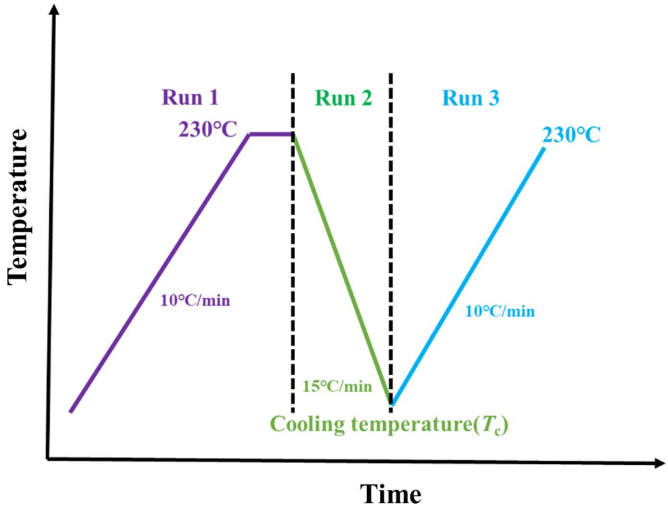

Figure 1
Diagrammatic sketch of the investigation of the probability of fracture and crystallization.

15°C min^{-1} to the different desired target cooling temperatures (T_c = −30, −20, −10, 0, 10, 20 and 30°C). The resulting amorphous samples were reheated to 230°C at a heating rate of 10°C min^{-1} to study the recrystallization probability (Run 3). Formation of fractures can be determined by a sharp exothermal peak in Run 2. Fifteen samples were measured for each T_c.

2.4. Measurement of crystal growth morphologies and kinetics of GSF in the presence of 10%(*w*/*w*) PVP K90

The morphologies of GSF crystals grown in PVP K90-doped GSF systems were acquired by using a polarized microscopy equipped with a hot stage to precisely control the temperature. Approximately 3 mg of PVP-doped physical mixtures were melted between two round cover slips at 230°C for 3 min and then quenched to room temperature. The crystal growth kinetics of GSF in the PVP K90-doped systems were obtained by measuring the advancing speed of a crystal front as a function of time. Crystal growth rates were obtained at temperatures from 110 to 180 °C. The reported rates in the present work were the average of four independent measurements.

2.5. Raman microscopy

Polymorphs of GSF in the PVP K90-doped systems were identified with a ThermoFisher DXR Raman microscope with a near-IR (780 nm) laser. A 50× objective was used and the laser power was 8 mW. Spectra were obtained by using an exposure time of 2 s for 30 measurements. As identified by Raman microscopy, all the GSF crystals grown and PVP K90-doped GSF systems were the thermodynamically stable form (form I; Section 3.4).

2.6. Dielectric measurement

Dielectric spectra of the PVP K90-doped GSF systems were obtained by using a Novocontrol Alpha dielectric spectrometer. Dielectric measurements were performed in the temperature range of 88–145°C, over the frequency range of 10^{-1}–10^{6} Hz. Samples prepared by melt-quenching were measured between two 20 mm-diameter gold-plated copper electrodes. Polytetrafluoroethylene electrodes were used to confine the melted GSF samples to avoid the overflow of the samples from the edge.

Complex dielectric permittivity $\varepsilon^*(\omega)$ was measured as a function of angular frequency ω and temperature T. Herein, ε^* consisted of the real part ε' and imaginary part ε''. To determine the average relaxation times (τ_{HN}), the dielectric loss spectra were analyzed by the Havriliak−Negami function plus d.c. conductivity term.

$$\varepsilon^*(\omega) = \varepsilon'(\omega) - i\varepsilon''(\omega) = \varepsilon_\infty + \frac{\varepsilon_s - \varepsilon_\infty}{[1 + (i\omega\tau_{HN})^\alpha]^\beta} + \frac{\sigma_{dc}}{i\omega\varepsilon_0}, \quad (1)$$

where ε_∞ is the high-frequency limit permittivity and ε_s is the static dielectric constant. α and β are the asymmetry and width of the dielectric peaks, respectively. $\sigma_{dc}/(i\omega\varepsilon_0)$ represents the conductivity component. σ_{dc} is the level of d.c. conductivity and ε_0 is the vacuum permittivity.

The α-relaxation time (τ_α) represents the relaxation time at a maximum loss (τ_{max}). The value of τ_α was calculated by the following equation on the basis of the parameters obtained by the Havriliak−Negami function:

$$\tau_\alpha = \tau_{max} = \tau_{HN}\left[\sin\left(\frac{\pi\alpha}{2+2\beta}\right)\right]^{-1/\alpha}\left[\sin\left(\frac{\pi\alpha\beta}{2+2\beta}\right)\right]^{1/\alpha}. \quad (2)$$

3. Results and discussion

3.1. Effects of PVP K90 on fracture and its connections with crystallization

The solids of small-molecule drugs are relatively fragile and have been reported to be modified by polymer additives (Chen *et al.*, 2017). One aim of the present study was to explore the effect of 10%(*w*/*w*) PVP K90 on the fracture resistance of amorphous GSF. More importantly, the connections between fracture and crystal nucleation of GSF were also tested in the presence of 10%(*w*/*w*) PVP K90. Fig. 2 shows DSC traces of GSF in or without the presence of 10%(*w*/*w*) PVP K90. In Run 1, crystals of GSF were heated at 10°C min^{-1} and melted at ∼219.2°C, showing a fusion heat of 115.3 J g^{-1}. For Run 2, the melt GSF was cooled with a cooling rate of 15°C min^{-1}. For the cooling process, the glass transition and an abrupt heat release of fracture were clearly observed. Herein, T_{frac} represents the temperature for the heat release of fracture. The exothermal peak at T_{frac} represents excess enthalpy stored as the glass solids were cooled under stress in comparison with the free-standing film (Chen *et al.*, 2017). In Run 3, the fractured GSF glass was reheated with a heating rate of 10°C min^{-1}. Glass-to-liquid transition and exothermic peaks related to the crystallization were observed. Different locations and proportions of exothermic peaks indicate the formation of different crystalline forms (pure form I or a mixture of forms II and III).

Table 1
Results of a statistical study of the link between fracture and crystal nucleation for pure GSF systems.

Chosen temperature	Fractured and crystallized	Not fractured and not crystallized	Fractured and not crystallized	Not fractured and crystallized	Total
−30°C	15	0	0	0	15
−20°C	15	0	0	0	15
−10°C	14	0	1	0	15
0°C	10	4	1	0	15
10°C	1	11	0	3	15
20°C	0	14	0	1	15
30°C	0	14	0	1	15

Table 2
Results of a statistical study of the link between fracture and crystal nucleation for GSF systems containing 10%(*w*/*w*) PVP K90.

Chosen temperature	Fractured and crystallized	Not fractured and not crystallized	Fractured and not crystallized	Not fractured and crystallized	Total
−30°C	9	0	6	0	15
−20°C	8	0	7	0	15
−10°C	6	3	2	4	15
0°C	2	5	1	7	15
10°C	0	6	0	9	15
20°C	0	9	0	6	15
30°C	0	12	0	3	15

Form I of GSF can be spontaneously nucleated at the free surface, while form II was spontaneously formed in the interior of amorphous GSF (Shi & Cai, 2016; Su *et al.*, 2018). Form II exhibited a slow growth rate and form III can cross-nucleate on form II (Su *et al.*, 2018). For the pure GSF, the measured glass transition temperature T_g was ∼88.1°C and the average fracture temperature (T_{fract}) was ∼7°C. PVP K90 exhibited a high T_g at ∼178°C. In the presence of 10%(*w*/*w*) PVP K90, the GSF system exhibited a higher T_g (∼90.2°C) and lower T_{fract} (∼−6.1°C). This indicates that 10% PVP K90 anti-plasticized the system and effectively increased system fracture resistance. Similar results were also reported in *o*-terphenyl glasses doped with 10% polystyrene (Chen *et al.*, 2017).

A statistical study was performed to test the fracture-induced nucleation and the effects of 10%(*w*/*w*) PVP K90. A large number of pure and polymer-doped GSF systems were cooled to various target temperatures (T_c = 30, 20, 10, 0, −10, −20, −30°C) and the performance upon heating was assessed. Tables 1 and 2 show the results for pure and PVP K90-doped GSF systems, respectively. For each T_c, a total of 15 samples were used for analysis. Based on the occurrence of fracture and crystallization, four behavior categories were obtained: (1) fractured and crystallized, (2) not fractured and not crystallized, (3) fractured and not crystallized, and (4) crystallized and not fractured.

For pure GSF systems, once the fracture occurred, all GSF samples exhibited recrystallization at lower T_c (−30 and −20°C). At the intermediate T_c (−10 and 0°C), the GSF samples mainly behaved as 'fractured and crystallized' and 'not fractured and not crystallized' systems. Only 2 of these 30 samples for intermediate T_c (−10 and 0°C) fractured and exhibited no crystallization. For the higher T_c (10, 20 and 30°C), most of the GSF samples behaved as 'not fractured and not crystallized'. Only one sample was 'fractured and crystallized'. The residual 5 samples of these 45 samples for T_c (10, 20 and 30°C) exhibited crystallization without the occurrence of fracture. Therefore, it can be concluded that most of the fractured GSF samples crystallized while unfractured samples did not. Only 7 of 115 samples were contrary to the above conclusion. These results support the view that crystal nucleation can be significantly enhanced by cooling the liquid to cause fracture (Su *et al.*, 2019). Fracture was expected to generate a free surface, providing the sites for heterogeneous nucleation and enhanced molecular mobility (Shi, Tao *et al.*, 2020; Shi *et al.*, 2021; Su *et al.*, 2019).

We also tested the connection between fracture and nucleation of griseofulvin in the presence of 10%(*w*/*w*) PVP

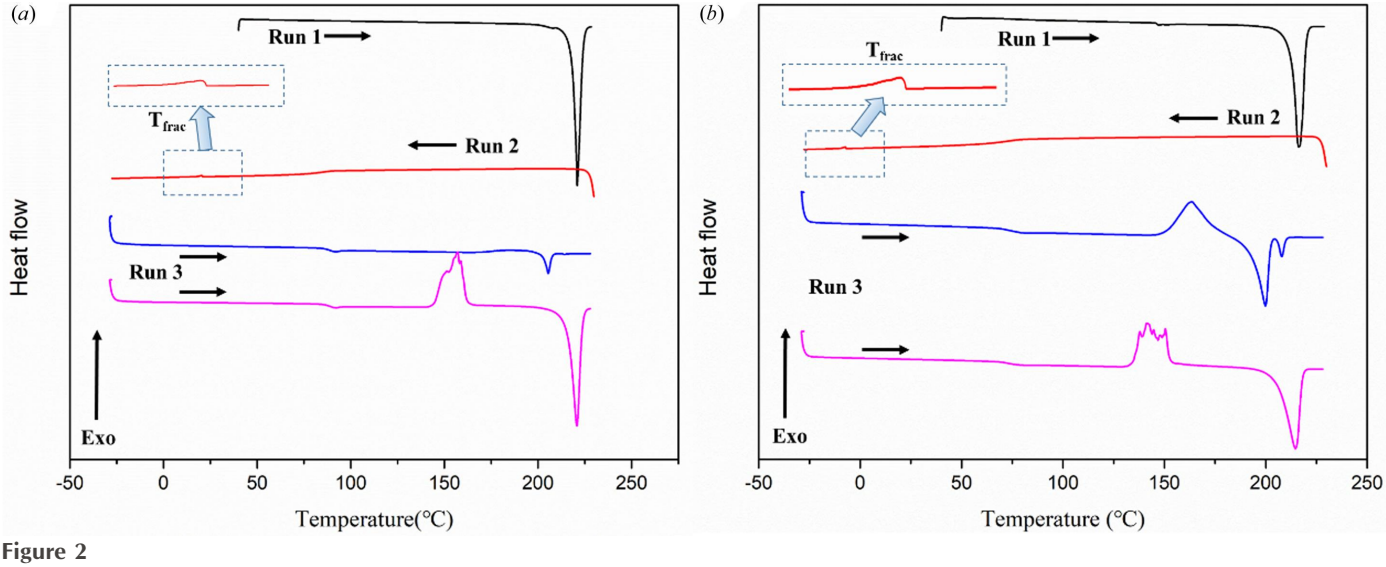

Figure 2
DSC traces of GSF (*a*) in or (*b*) without the presence of 10% PVP K90 for T_c = −30°C.

K90. For the 30 samples for lower T_c (−30 and −20°C), all the samples were fractured. Unlike the pure GSF systems, 13 of these 30 fractured samples of GSF doped with 10% PVP K90 exhibited no crystallization during the following heating process. These results were mainly attributed to the significantly inhibitory effects of PVP on the nucleation and crystal growth of amorphous drugs (Powell *et al.*, 2015; Zhang, Liu *et al.*, 2021). Even though fracture occurred, the presence of PVP K90 also effectively maintained the amorphous form of GSF. At the intermediate T_c (−10 and 0°C), the connections between fracture and nucleation were further disrupted for the PVP K90-doped GSF systems. For the higher T_c (10, 20 and 30°C), the ratio of 'not fractured and not crystallized' samples increased with an increase in T_c. In contrast, the ratio of 'not fractured and crystallized' decreased as T_c increased from 10 to 30°C. These results indicate that thermal history in the glassy state in addition to the fracture was an important factor for determining the crystal nucleation.

Fig. 3(*a*) summarizes the probability of fracture as a function of target cooling temperature (T_c) for pure and PVP K90-doped GSF systems. At the lower T_c (−30 and −20°C), both the pure and the PVP K90-doped GSF systems were fractured. For the intermediate T_c (−10, 0 and 10°C), the probability of fracture for pure GSF systems was much higher than that of PVP K90 GSF systems. It is argued that PVP K90 effectively increased the resistance of amorphous GSF against fracture. For the higher T_c (20 and 30°C), no fractured samples were observed for either pure or PVP K90-doped GSF systems. We also compared the probability of the occurrence of crystallization for the fractured samples of pure and PVP K90-doped GSF systems. As shown in Fig. 3(*b*), crystallization occurred for almost all the fractured samples (∼96.1%) of pure GSF systems. For comparison, nearly 63.8% of fractured samples of PVP K90-doped systems crystallized. These results indicate that the addition of PVP K90 also inhibited the crystal nucleation for the fractured samples.

Fracture can induce the formation of micro-cracks and trigger crystal nucleation and crystal growth (Shi, Tao *et al.*, 2020; Thakore *et al.*, 2024; Willart *et al.*, 2017). This explains the puzzling 'anomalous' nucleation in molecular glasses. In addition, a very recent study reported that cracked samples exhibited relatively inhomogeneous mechanical properties (Thakore *et al.*, 2024). From the perspective of physical stability, tensile fracture-triggered enhanced crystal nucleation should be considered as one important factor for affecting drug crystallization in the glassy state. Proximity to the surface or an interface had been widely reported to accelerate the nucleation and crystal growth of amorphous pharmaceutical solids (Zhang, Xu *et al.*, 2023; Newman & Zografi, 2021; Shi, Moinuddin *et al.*, 2022; Yao, Liu *et al.*, 2022; Yao, Borchardt *et al.*, 2022). Our results show that PVP K90 affected both fracture and the subsequent crystallization process. It was expected that PVP K90 would also have significant effects on inhibiting the nucleation and crystal growth at surfaces and interfaces.

3.2. Effects of 10%(*w*/*w*) PVP K90 on the crystallization of amorphous griseofulvin

GSF was first isolated from *Penicillium griseofulvum* in 1939 and was recently found to have bioactivity towards a range of mammalian cancer cell lines (Petersen *et al.*, 2014). The first crystal structure of GSF (form I) was identified in 1977 by the classical method of solution crystallization. In 2013, Mahieu *et al.* (2013) reported two new metastable polymorphs from GSF melts, as shown by their distinct melting points (T_m) and powder X-ray diffraction patterns compared with those of form I. The crystal structures of these two metastable polymorphs of GSF were eventually resolved from the melt in recent studies (Su *et al.*, 2018; Ou *et al.*, 2020). Su *et al.* (2018) successfully obtained a single crystal of form II of GSF by accelerating its crystal growth when doped with low-concentration poly(ethylene oxide). They also reported that

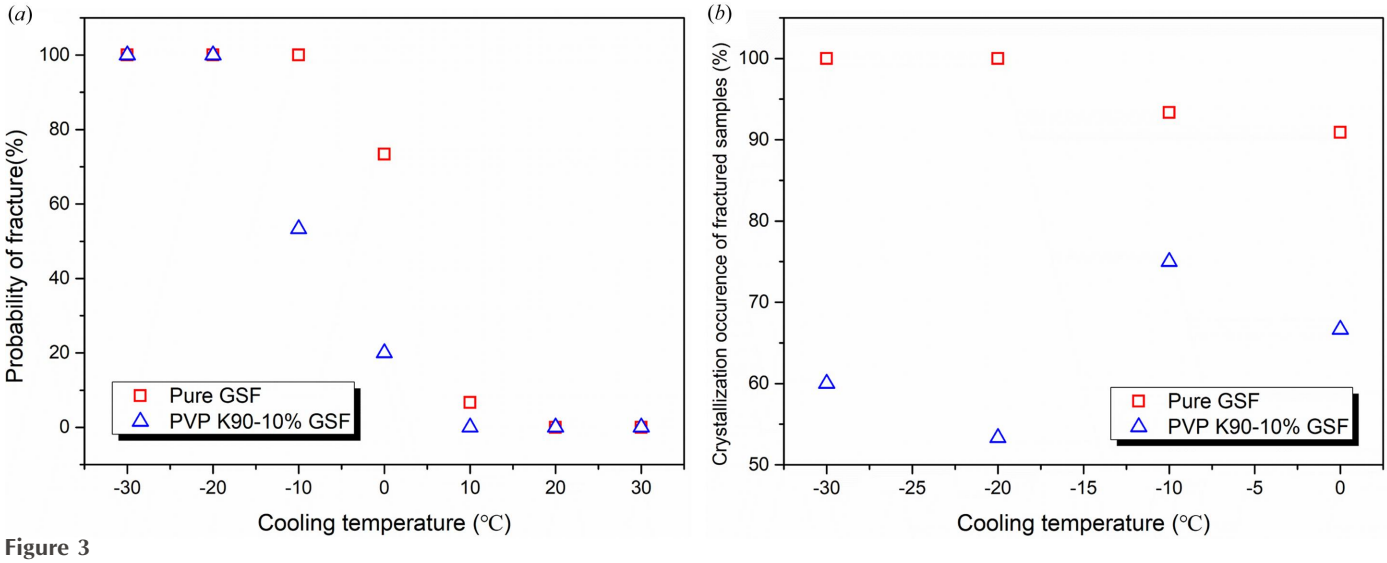

Figure 3
(*a*) Probability of fracture as a function of cooling temperature for pure and PVP K90-doped GSF systems. (*b*) Probability of crystallization occurrence of fractured samples.

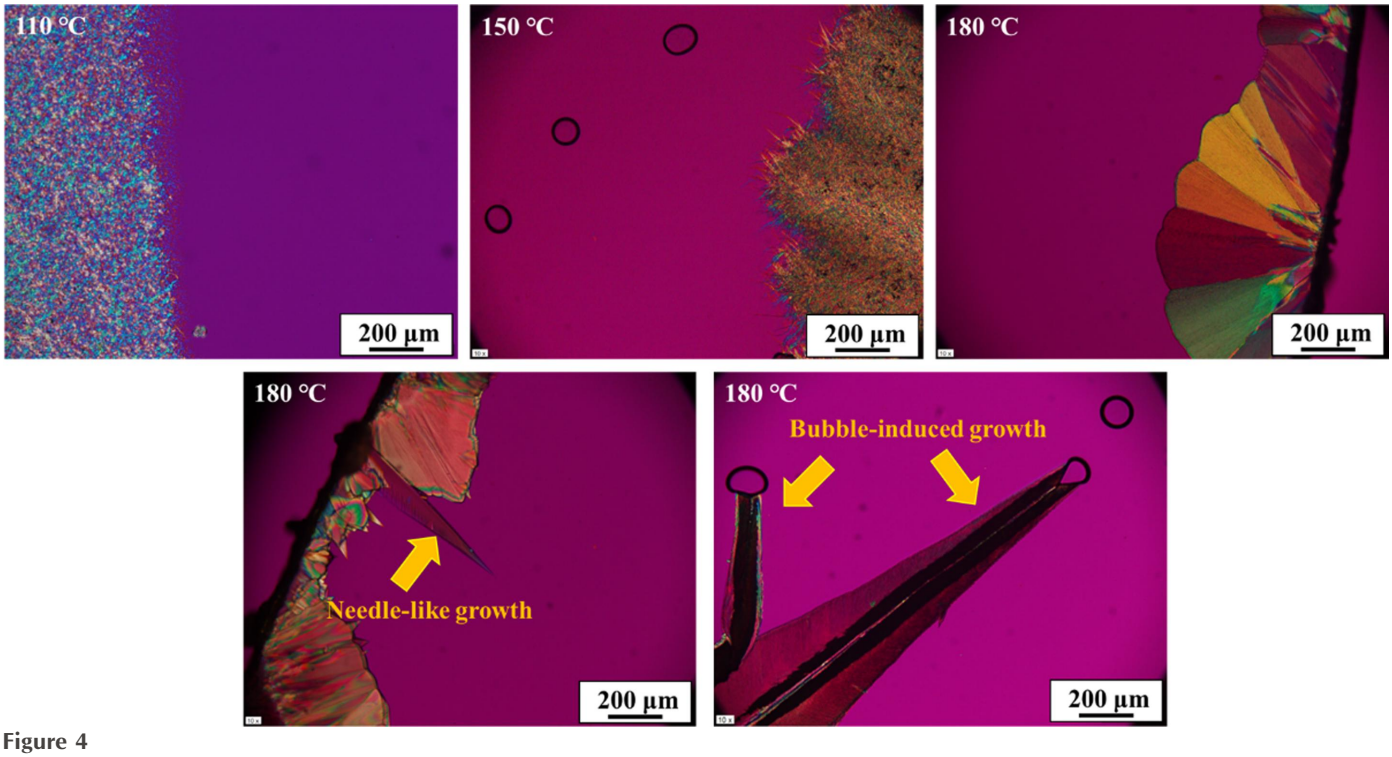

Figure 4
Growth morphologies of griseofulvin in the presence of 10%(*w*/*w*) PVP K90.

form II of GSF had an anomalously large coefficient of thermal expansion (Su *et al.*, 2018). Missing structural information of GSF form III was identified by a creative strategy of rapidly growing a single crystal from melted micro-droplets (Ou *et al.*, 2020). Compared with forms II and III, GSF form I exhibited a much faster crystal growth velocity (Su *et al.*, 2018).

In the present study, all bulk crystals of GSF were identified as thermodynamically stable form I.

Fig. 4 shows the morphologies of GSF bulk crystals in the supercooled liquid of PVP K90-doped amorphous systems. For pure GSF systems, crystals grew in the form of fibers near T_g, while they grew as compact spherulites with an increase in temperature (Shi & Cai, 2016). Similar growth morphologies were also observed in the presence of 10%(*w*/*w*) PVP K90. Fiber growth is considered as a precursor of glass-to-crystal (GC) growth when heating a liquid near or above T_g, as widely reported in several organic systems that show GC growth (Shi & Cai, 2016; Shi, Wang, Xu *et al.* 2022; Sun, Xi, Ediger *et al.*, 2008). In our previous study, we found that the fiber growth of GSF can persist at a temperature up to nearly $1.15T_g$. In the present study, fiber growth of GSF in PVP K90-doped systems is seen to persist to a higher temperature in comparison with the pure GSF systems. Given that PVP K90 exhibited a high T_g at nearly 178°C, it was expected that the addition of 10%(*w*/*w*) PVP K90 would significantly increase the system T_g. This is indeed the case: thermal analysis showed that T_g of GSF in the presence of 10%(*w*/*w*) PVP K90 can increase to ∼90.2°C. However, the increase in system T_g was not sufficient for explaining the persistence of fiber growth of GSF to such high temperatures in the presence of PVP K90. What distinguished PVP-doped GSF systems from pure GSF systems was that GSF crystal growth in the PVP-doped systems exhibited an anomalously rapid needle-like growth.

Fig. 5 shows the crystal growth kinetics of GSF in pure and PVP K90-doped systems as a function of temperature. The velocities of crystal growth of GSF were significantly reduced when doped with 10%(*w*/*w*) PVP K90. For instance, compared with the pure GSF systems, the addition of 10%(*w*/*w*) PVP K90 yielded a ∼28.1-fold decrease in the velocities of crystal growth at 110°C. When the temperature is increased to 150°C, the inhibitory effects of PVP K90 weaken, yielding a ∼4.8-fold

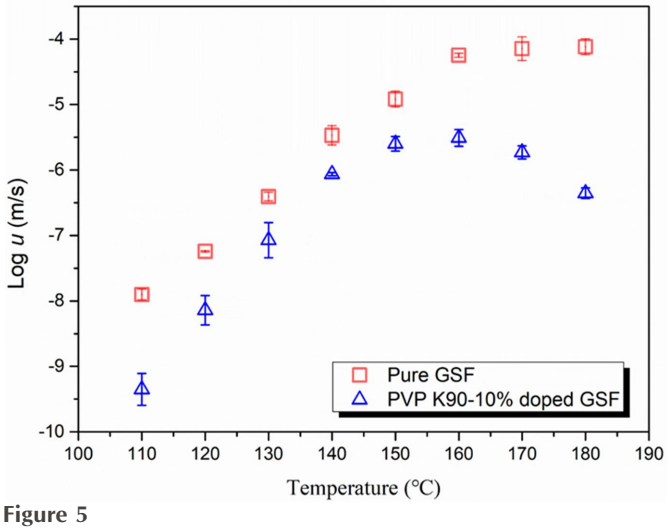

Figure 5
Crystal growth rates of pure and 10%(*w*/*w*) PVP K90-doped GSF systems as a function of temperature.

decrease in crystal growth rate. A further increase in the temperature would lead to more significant inhibitory effects of PVP K90 on the crystal growth. Moreover, the crystal growth kinetics of pure and PVP K90-doped amorphous systems exhibited different temperature dependences. For the pure GSF systems, crystal growth rates smoothly increased when heating the liquid from 110 to 180°C. However, the velocity of crystal growth in PVP K90-doped systems first increased with an increase in temperature and then decreased.

For pure drug systems, crystal growth velocities were found to be governed by thermodynamic driving forces near T_m while being mainly governed by bulk diffusion in deep supercooled liquid (Swallen & Ediger, 2011). A bell-shaped curve of the velocities of crystal growth with a maximum value was observed (Shi & Cai, 2016; Sun, Xi, Chen *et al.*, 2008; Tian *et al.*, 2017). In the present study, the addition of 10%(*w*/*w*) PVP K90 lowered the temperature of the maximum velocity of crystal growth of GSF. A similar result was also reported in polymer-doped indomethacin systems (Tian *et al.*, 2017). With the addition of 10%(*w*/*w*) hydroxypropyl methylcellulose, the temperature corresponding to the maximum crystal velocity of the α-form of indomethacin exhibited an evident decrease from 135 to 100°C (Tian *et al.*, 2017). The addition of PVP K90 can affect both the thermodynamic and kinetic factors for controlling the crystal growth of GSF. It was expected that crystal growth of GSF in the presence of PVP K 90 would enter the thermodynamic-driving-force-controlled region at a lower temperature. Compared with the pure GSF system, GSF in PVP K90-doped systems exhibited much stronger temperature dependence in the diffusion-controlled region. It was expected that the addition of PVP K90 would increase the activation energy of crystal growth of GSF. As shown in Fig. 6, the crystal growth of pure GSF and PVP K90-doped GSF systems was of Arrhenius type. The calculated activation energy of crystal growth of pure GSF systems was 240.3 K J mol^{-1}. With the addition of 10% PVP K90, the activation energy was increased to 298.7 K J mol^{-1}. Similar results have also been reported in GSF systems doped with acetylated maltose (Madejczyk *et al.*, 2019).

3.3. Effects of 10%(*w*/*w*) PVP K90 on liquid dynamics of amorphous griseofulvin

Molecular mobility is generally accepted as one of the most reliable predictors for the crystallization of amorphous forms (Grzybowska *et al.*, 2016). Dielectric spectroscopy is a well established technique that can distinguish global and local molecular mobility. It has been widely used to examine different relaxation processes that might be responsible for physical stability (Grzybowska *et al.*, 2016; Kothari *et al.*, 2014; Fung *et al.*, 2018). In order to understand the inhibitory effects of PVP K90, the molecular mobility of GSF in the presence of 10%(*w*/*w*) PVP K90 was investigated by using broadband dielectric spectroscopy. Fig. 7 shows the dielectric loss behaviors of GSF systems doped with 10%(*w*/*w*) PVP K90 as a function of temperature. With increasing temperature, well resolved peaks shifted towards higher frequencies. These peaks have previously been demonstrated in several studies to be attributable to the α-relaxation, a measure of global molecular mobility that strongly relates to the glass transition and viscous flow (Grzybowska *et al.*, 2016; Li *et al.*, 2021). The dielectric loss spectra of GSF exhibited a single α-relaxation peak with the addition of 10%(*w*/*w*) PVP K90, indicating the homogeneous nature.

Fig. 8 shows the α-relaxation times in pure and PVP K90-doped GSF systems as a function of temperature. As expected, the temperature dependence was nonlinear and can be well described by the following empirical Vogel–Fulcher–Tammann equation:

$$\tau_\alpha = \tau_0 \exp\left(\frac{DT_0}{T - T_0}\right). \quad (3)$$

In this equation, τ_α represents the α-relaxation time and τ_0 the relaxation time of the unrestricted material. D represents the

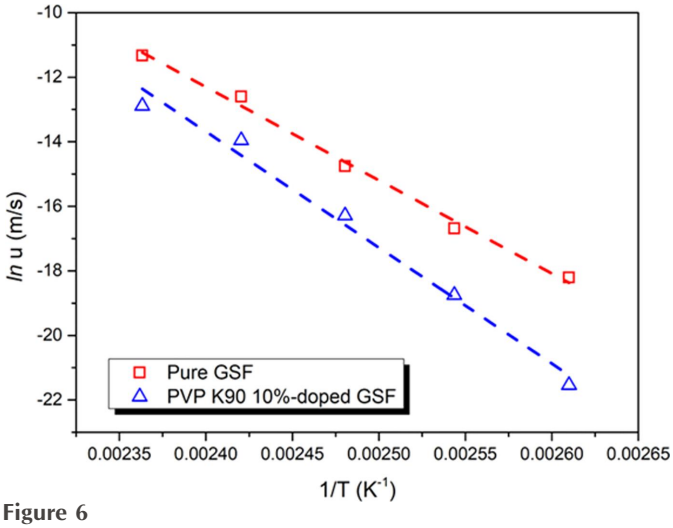

Figure 6
Arrhenius kinetics of crystal growth for pure and 10% PVP K90-doped GSF systems.

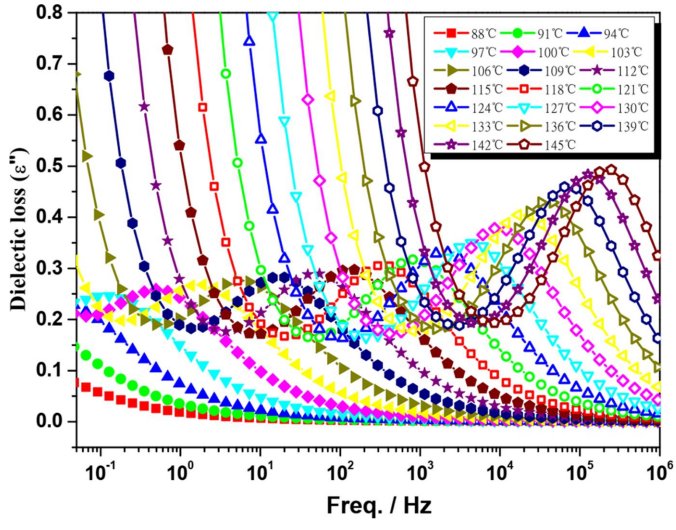

Figure 7
Dielectric loss of GSF in the presence of 10%(*w*/*w*) PVP K90 as a function of temperature.

Table 3
Values of T_g (from DSC and dielectric measurement) for pure and 10%(*w*/*w*) PVP K90-doped GSF systems.

Substance	GSF	10%(*w*/*w*) PVP K90-doped systems
T_g(DSC)	88.1°C	90.2°C
T_g(dielectric measurement)	85.9°C	89.1°C

strength parameter as a measure of fragility and T_0 represents the zero-mobility temperature. As shown in the inset of Fig. 8, the α-relaxation peak of GSF moved to a lower frequency with the addition of 10%(*w*/*w*) PVP K90, indicating that PVP K90 can significantly decrease system molecular mobility. Moreover, doping with 10%(*w*/*w*) PVP K90 caused a significant increase of α-relaxation time over the full experimental temperature range.

Table 3 compares the values of T_g obtained from DSC and dielectric measurements for pure and 10%(*w*/*w*) PVP K90-doped GSF systems. With the addition of PVP K90, the T_gs obtained from both DSC and dielectric measurement exhibited a progressive increase. Herein, T_gs obtained from dielectric measurements were defined as the temperature at which τ_α = 100 s. A good agreement was observed in the T_gs obtained from DSC and dielectric measurements. Similar results have also been observed in GSF doped with acetylated maltose and poly(ethylene oxide) (Madejczyk *et al.*, 2019; Shi, Zhang, Su *et al.*, 2017).

Fig. 9 shows the crystal growth rates of GSF in pure and PVP K90-doped GSF systems as a function of α-relaxation times in the log–log format. The linear correlations between crystal growth rates and α-relaxation times were investigated by using the following equation:

$$\log_{10} u = -\xi \log_{10} \tau_\alpha + A, \quad (4)$$

where ξ represents the coupling relationship between crystal growth rates and α-relaxation times and A is a fitting parameter. Crystal growth in a single-component supercooled liquid was generally accepted to be mainly controlled by the thermodynamic driving force near T_m and bulk diffusion far away from T_m (Shi, Li *et al.*, 2020). From the perspective of crystal growth dynamics, growth rates were determined by two key factors, namely the velocities of molecules transporting into the crystalline phase and the probability of the newly formed crystal irreversibly joining the crystalline phase (Ediger *et al.*, 2008). In the presence of polymer or small-molecule additives, the mechanism of crystal growth in the binary system becomes more complex (Zhang *et al.*, 2017; Shi, Zhang, Su *et al.*, 2017; Zhang *et al.*, 2019; Zhang, Shi *et al.*, 2021). Besides the overall liquid dynamics or thermodynamic effects, polymers tended to enrich at the growth front and also play a controlling role in the crystal growth of amorphous drugs (Shi, Zhang, Su *et al.*, 2017; Zhang *et al.*, 2019). In studies of poly(ethylene oxide)-doped amorphous drug systems, the increased overall molecular mobility was not sufficient to explain the accelerating effects of the polymer on the crystallization of the amorphous drug (Zhang, Shi *et al.*, 2021; Shi, Zhang, Zhang *et al.*, 2017). This fact is evident because of the non-overlapping of crystal growth velocities in pure and poly(ethylene oxide)-doped amorphous systems at the α-relaxation timescale (Zhang, Shi *et al.*, 2021; Shi, Zhang, Zhang *et al.*, 2017). In the present work, GSF grown in pure and PVP K90-doped systems also exhibited different kinetics at the same scale of α-relaxation time. Therefore, it is proposed that the decreased overall molecular mobility cannot fully explain the crystallization inhibiting effects of PVP K90. Moreover, it was clearly observed that the coupling relationships between crystallization and liquid dynamics were altered in the presence of 10%(*w*/*w*) PVP K90. We speculate that PVP K90 could also affect the crystal–liquid interface, as reported above for poly(ethylene oxide), in addition to its effects on the liquid dynamics.

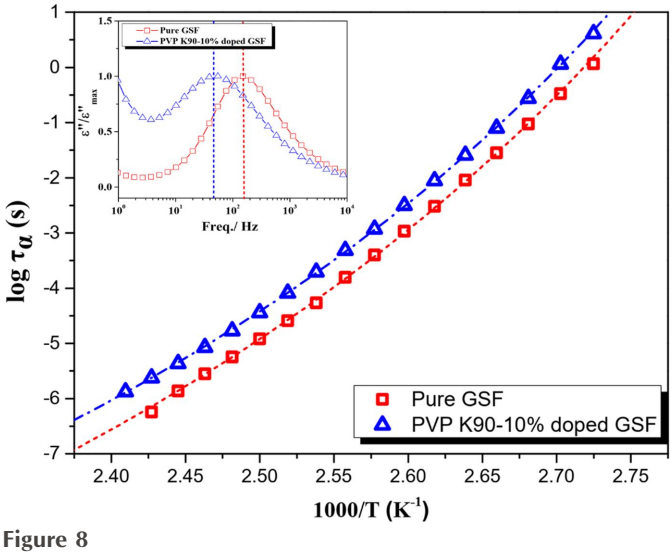

Figure 8
Temperature dependences of α-relaxation time of pure and 10%(*w*/*w*) PVP K90-doped GSF systems. The inset is a comparison of dielectric loss of pure and 10% PVP K90-doped GSF systems at 112°C.

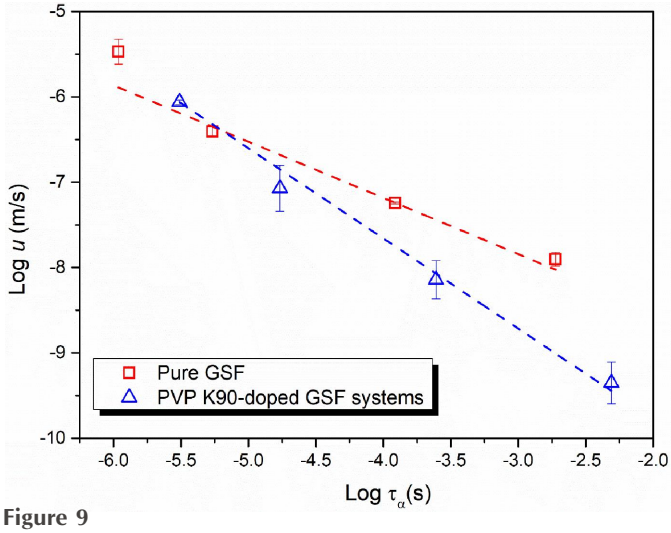

Figure 9
Crystal growth rate u plotted against the α-relaxation time in pure and 10%(*w*/*w*) PVP K90-doped GSF systems.

3.4. Formation of needle-like crystal growth in the presence of PVP K90

As mentioned above, GSF in PVP K90-doped systems can exhibit bubble-induced and needle-like crystal growth behaviors. Bubble-induced crystal growth in the interior of amorphous pharmaceuticals was first reported in griseofulvin at temperatures from 130 to 150°C (Shi, Tao *et al.*, 2020; Shi & Cai, 2016). In subsequent studies, these interesting growth behaviors have also been found in the crystal growth of nimesulide and in the γ-form and α-form of indomethacin (Shi *et al.*, 2021; Shi, Wang, Xu *et al.*, 2022). This enhanced crystallization through the air–liquid interface was mainly attributed to the fast molecular diffusion at the surface and interface (Yu, 2016; Huang, Ruan *et al.*, 2017). It is widely accepted that molecules at the surface will exhibit different dynamics and organization compared with those in the bulk. As a result, nucleation, polymorphs and crystal growth can be altered at the surface and interface (Zhang, Xu *et al.*, 2023; Sun *et al.*, 2012; Shi, Moinuddin *et al.*, 2022; Yao, Liu *et al.*, 2022). For instance, nucleation rates of clotrimazole polymorphs at the surface can be vastly accelerated by 5–6.5 orders of magnitude in comparison with those in the bulk (Zhang, Xu *et al.*, 2023). Moreover, surface-accelerating effects on the nucleation of clotrimazole form II were relatively more significant than those on form I. Surface effects also accelerated the crystal growth of clotrimazole polymorphs. A greater accelerating effect induced by the surface can be observed on clotrimazole form I in comparison with form II. These accelerating effects on nucleation were mainly originated from the specific surface molecular structure and fast surface dynamics. Yao, Liu *et al.* (2022) reported that nucleation of D-arabitol at the free surface was much faster than nucleation in the interior, by 12 orders of magnitude on a per-molecule basis (Yao, Liu *et al.*, 2022). More importantly, D-arabitol nucleated as form II at the free surface but as form I in the bulk. This phenomenon was a consequence of the similarity of the molecular structure of surface-nucleating form II and the surface molecular packing (Yao, Liu *et al.*, 2022).

For pure GSF systems, the termination of bubble-induced crystal growth below 130°C was mainly attributed to the high viscosity, which could effectively prevent the advancing movement of bubbles (Shi, Tao *et al.*, 2020). Unlike in the pure GSF systems, bubble-induced crystal growth of GSF in the presence of 10%(*w*/*w*) PVP K90 was terminated as the temperature decreased to 150°C. These results were mainly attributed to the increase in system viscosity with the addition of 10%(*w*/*w*) PVP K90. Moreover, bubble-induced crystallization of GSF in the presence of 10%(*w*/*w*) PVP K90 extended to much higher temperature (~190°C). As previously reported, the polymer exhibited weaker effects on the crystal growth at the free surface compared with those in the interior (Powell *et al.*, 2013). Here, the inhibitory effects of PVP K90 on the surface crystal growth of GSF were vastly reduced in comparison with those on the bulk crystal growth. Thus, surface and bulk crystal growth can be decoupled at higher temperature, facilitating bubble-induced growth behavior.

In addition to the bubble-induced crystal growth, GSF crystals could rapidly grow in the needle-like form in the presence of PVP K90. Fig. 10 shows the advancing distance of a crystal growth front as a function of time for the bubble-induced, needle-like and normal bulk crystal growth of GSF in the presence of 10%(*w*/*w*) PVP K90 at 180°C. Needle-like crystal growth was much faster than the normal bulk crystal growth. In addition, the velocity of needle-like crystal growth was comparable to that of bubble-induced crystal growth. Recent studies proposed that bubble-induced growth was a surface-facilitated process (Shi, Tao *et al.*, 2020; Shi *et al.*, 2021; Shi, Wang, Xu *et al.*, 2022). Bubbles generated from the crystallization provided an air–liquid interface to accelerate the crystal growth, taking advantage of the high surface mobility (Yu, 2016). However, needle-like crystal growth seemed irrelevant to the surface-facilitated process since we cannot observe any evidence of the existence of the air–liquid interface. Powell *et al.* (2015) proposed that GC growth was also a surface-facilitated process without the microscopic free surface. GC growth, one anomalously rapid crystal growth behavior of some organic molecules, was speculated to continuously produce small voids and free surfaces to sustain the crystal growth (Powell *et al.*, 2015). Interestingly, GC growth can persist in fast-growing fibers up to approximately $1.15T_g$ in a supercooled liquid (Sun *et al.*, 2008). Some fibers deeply extended into the supercooled liquid while other fibers slowly filled the crystal growth front. This fast fiber growth was considered as the precursor of GC growth, as shown by the linear growth rates for these two growth modes with no discontinuity.

In the present work, the morphologies of needle-like growth were similar to the previously reported fiber growth to some extent. Unlike in pure GSF systems, needle-like growth of GSF in the presence of PVP K90 can occur at higher temperatures. We speculate that needle-like crystal growth

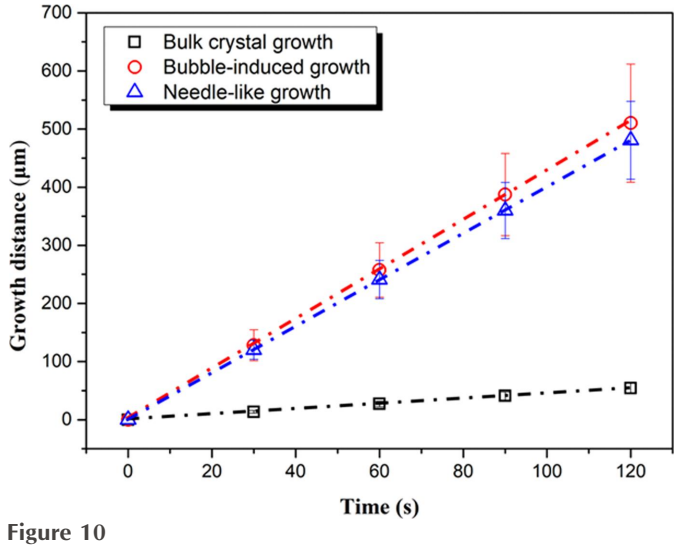

Figure 10
Growth distance of bubble-induced growth, needle-like growth and normal bulk growth of GSF in the presence of 10%(*w*/*w*) PVP K90 as a function of time at 180°C.

was also a surface-facilitated process. This view is strongly supported by the fact that needle-like growth exhibits approximately the same velocities as bubble-induced growth. Analogously to GC growth, needle-like growth might also depend on the small voids or bubbles at the crystal growth front. It has been widely reported that a polymer rejected during the crystal growth process would enrich the growth front (Powell *et al.*, 2013; Huang, Powell *et al.*, 2017; Zhang *et al.*, 2017, 2019). This polymer enrichment was also expected to affect the microstructure and facilitate the formation of small voids or bubbles. However, the underlying mechanism of needle-like crystal growth in PVP-doped GSF systems remains a significant question.

4. Conclusions

The addition of PVP K90 yielded a significant change in molecular mobility, crystal growth, fracture, and connections between fracture and crystal nucleation. The fracture resistance of griseofulvin was greatly improved in the presence of PVP K90. The direct connection between fracture and nucleation of griseofulvin can be significantly weakened with the addition of PVP K90. Crystal growth and the molecular mobility of GSF can also be slowed down in the presence of PVP K90. In addition, in the presence of PVP K90, needle-like crystal growth of GSF can be triggered and exhibited approximately the same rates as bubble-induced growth. These results cannot be fully explained by the change in the liquid dynamics of amorphous solids. Future work should further investigate the mechanism of physical stability of polymer-based amorphous solid dispersions from different perspectives, including surface-facilitated and surface/interface-facilitated processes and polymer-induced changes in liquid dynamics.

Acknowledgements

The authors declare no competing financial interests.

Funding information

The authors are grateful for the financial support of this work by the Natural Science Foundation of Jiangsu Province (No. BK20211114), General Medical Research Projects of Jiangsu Commission of Health (No. H2023070), Key Medical Research Projects of the Health Commission of Yancheng (No. YK2023031), Scientific and Technological Innovation Team Project of Jiangsu Vocational College of Medicine (grant No. 20234302), Excellent Teaching Team of 'Qinglan Project' in Jiangsu Province, and Jiangsu Higher Education Institution Innovative Research Team for Science and Technology (2023).

References

Cai, T., Zhu, L. & Yu, L. (2011). *Pharm. Res.* **28**, 2458–2466.
Chen, Y., Powell, C. T. & Yu, L. (2017). *J. Phys. Chem. B*, **121**, 444–449.
Ediger, M. D., Harrowell, P. & Yu, L. (2008). *J. Chem. Phys.* **128**, 034709.
Fung, M. H., DeVault, M., Kuwata, K. T. & Suryanarayanan, R. (2018). *Mol. Pharm.* **15**, 1052–1061.
Grzybowska, K., Capaccioli, S. & Paluch, M. (2016). *Adv. Drug Deliv. Rev.* **100**, 158–182.
Huang, C., Powell, C. T., Sun, Y., Cai, T. & Yu, L. (2017). *J. Phys. Chem. B*, **121**, 1963–1971.
Huang, C., Ruan, S., Cai, T. & Yu, L. (2017). *J. Phys. Chem. B*, **121**, 9463–9468.
Kalepu, S. & Nekkanti, V. (2015). *Acta Pharm. Sin. B*, **5**, 442–453.
Kestur, U. S. & Taylor, L. S. (2010). *CrystEngComm*, **12**, 2390–2397.
Kestur, U. S. & Taylor, L. S. (2013). *Cryst. Growth Des.* **13**, 4349–4354.
Konno, H., Handa, T., Alonzo, D. E. & Taylor, L. S. (2008). *Eur. J. Pharm. Biopharm.* **70**, 493–499.
Kothari, K., Ragoonanan, V. & Suryanarayanan, R. (2014). *Mol. Pharm.* **11**, 3048–3055.
Li, F., Xin, J. & Shi, Q. (2021). *J. Appl. Cryst.* **54**, 142–147.
Madejczyk, O., Minecka, A., Kamińska, E., Heczko, D., Tarnacka, M., Wolnica, K., Kamiński, K. & Paluch, M. (2019). *Cryst. Growth Des.* **19**, 1031–1040.
Mahieu, A., Willart, J. F., Dudognon, E., Eddleston, M. D., Jones, W., Danède, F. & Descamps, M. (2013). *J. Pharm. Sci.* **102**, 462–468.
Mistry, P. & Suryanarayanan, R. (2016). *Cryst. Growth Des.* **16**, 5141–5149.
Newman, A. & Zografi, G. (2021). *Mol. Pharm.* **19**, 378–391.
Orszulak, L., Lamrani, T., Tarnacka, M., Hachuła, B., Jurkiewicz, K., Zioła, P., Mrozek-Wilczkiewicz, A., Kaminska, E. & Kaminski, K. (2024). *Pharmaceutics*, **16**, 136.
Ou, X., Li, X., Rong, H., Yu, L. & Lu, M. (2020). *Chem. Commun.* **56**, 9950–9953.
Petersen, A. B., Rønnest, M. H., Larsen, T. O. & Clausen, M. H. (2014). *Chem. Rev.* **114**, 12088–12107.
Powell, C. T., Cai, T., Hasebe, M., Gunn, E. M., Gao, P., Zhang, G., Gong, Y. & Yu, L. (2013). *J. Phys. Chem. B*, **117**, 10334–10341.
Powell, C. T., Xi, H., Sun, Y., Gunn, E., Chen, Y., Ediger, M. D. & Yu, L. (2015). *J. Phys. Chem. B*, **119**, 10124–10130.
Pui, Y., Chen, Y., Chen, H., Wang, S., Liu, C., Tonnis, W., Chen, L., Serno, P., Bracht, S. & Qian, F. (2018). *Mol. Pharm.* **15**, 2754–2763.
Shi, Q. & Cai, T. (2016). *Cryst. Growth Des.* **16**, 3279–3286.
Shi, Q., Chen, H., Wang, Y., Wang, R., Xu, J. & Zhang, C. (2022). *Pharmaceutics*, **14**, 1747.
Shi, Q., Li, F., Xu, J., Wu, L., Xin, J., Chen, H. & Ling, B. (2021). *J. Appl. Cryst.* **54**, 1509–1513.
Shi, Q., Li, F., Yeh, S., Wang, Y. & Xin, J. (2020). *Int. J. Pharm.* **590**, 119925.
Shi, Q., Moinuddin, S. M., Wang, Y., Ahsan, F. & Li, F. (2022). *Int. J. Pharm.* **625**, 122098.
Shi, Q., Tao, J., Zhang, J., Su, Y. & Cai, T. (2020). *Cryst. Growth Des.* **20**, 24–28.
Shi, Q., Wang, Y., Moinuddin, S. M., Feng, X. & Ahsan, F. (2022). *AAPS PharmSciTech*, **23**, 259.
Shi, Q., Wang, Y., Xu, J., Liu, Z. & Chin, C.-Y. (2022). *Acta Cryst.* B**78**, 33–39.
Shi, Q., Zhang, C., Su, Y., Zhang, J., Zhou, D. & Cai, T. (2017). *Mol. Pharm.* **14**, 2262–2272.
Shi, Q., Zhang, J., Zhang, C., Jiang, J., Tao, J., Zhou, D. & Cai, T. (2017). *Mol. Pharm.* **14**, 4694–4704.
Su, Y., Xu, J., Shi, Q., Yu, L. & Cai, T. (2018). *Chem. Commun.* **54**, 358–361.
Su, Y., Yu, L. & Cai, T. (2019). *Cryst. Growth Des.* **19**, 40–44.
Sun, Y., Xi, H., Chen, S., Ediger, M. D. & Yu, L. (2008). *J. Phys. Chem. B*, **112**, 5594–5601.
Sun, Y., Xi, H., Ediger, M. D. & Yu, L. (2008). *J. Phys. Chem. B*, **112**, 661–664.

Sun, Y., Zhu, L., Wu, T., Cai, T., Gunn, E. M. & Yu, L. (2012). *AAPS J.* **14**, 380–388.
Swallen, S. F. & Ediger, M. D. (2011). *Soft Matter*, **7**, 10339–10344.
Taylor, L. S. & Zhang, G. G. Z. (2016). *Adv. Drug Deliv. Rev.* **101**, 122–142.
Thakore, S. D., Das, K., Dalvi, S. V., Reddy, C. M. & Bansal, A. K. (2024). *Mol. Pharm.* **21**, 76–86.
Tian, B., Gao, W., Tao, X., Tang, X. & Taylor, L. S. (2017). *Cryst. Growth Des.* **17**, 6467–6476.
Trasi, N. S. & Taylor, L. S. (2012*a*). *CrystEngComm*, **14**, 5188–5197.
Trasi, N. S. & Taylor, L. S. (2012*b*). *Cryst. Growth Des.* **12**, 3221–3230.
Willart, J. F., Dudognon, E., Mahieu, A., Eddleston, M., Jones, W. & Descamps, M. (2017). *Eur. Phys. J. Spec. Top.* **226**, 837–847.
Yao, X., Borchardt, K. A., Gui, Y., Guzei, I. A., Zhang, G. G. Z. & Yu, L. (2022). *J. Chem. Phys.* **157**, 194502.
Yao, X., Liu, Q., Wang, B., Yu, J., Aristov, M. M., Shi, C., Zhang, G. G. Z. & Yu, L. (2022). *J. Am. Chem. Soc.* **144**, 11638–11645.
Yu, L. (2001). *Adv. Drug Deliv. Rev.* **48**, 27–42.
Yu, L. (2016). *Adv. Drug Deliv. Rev.* **100**, 3–9.
Zhang, J., Guo, M., Luo, M. & Cai, T. (2023). *Asia. J. Pharm. Sci.* **18**, 100834.
Zhang, J., Liu, Z., Wu, H. & Cai, T. (2021). *Biomater. Sci.* **9**, 4308–4316.
Zhang, J., Shi, Q., Qu, T., Zhou, D. & Cai, T. (2021). *Int. J. Pharm.* **610**, 121235.
Zhang, J., Shi, Q., Tao, J., Peng, Y. & Cai, T. (2019). *Mol. Pharm.* **16**, 1385–1396.
Zhang, J., Xu, M., Wu, S., Chen, Z., Luo, L., Zi, T., Peng, X., Yang, Q., Liu, M. & Zeng, Z. (2023). *Cryst. Growth Des.* **23**, 3535–3543.
Zhang, S., Britten, J. F., Chow, A. H. L. & Lee, T. W. Y. (2017). *Cryst. Growth Des.* **17**, 3433–3442.